IOP Publishing New J. Phys. 26 (2024) 023059 https://doi.org/10.1088/1367-2630/ad2a82

New Journal of Physics
The open access journal at the forefront of physics

Deutsche Physikalische Gesellschaft DPG
IOP Institute of Physics

Published in partnership with: Deutsche Physikalische Gesellschaft and the Institute of Physics

OPEN ACCESS

RECEIVED
30 November 2023

REVISED
8 February 2024

ACCEPTED FOR PUBLICATION
19 February 2024

PUBLISHED
1 March 2024

PAPER

Nanoribbons of large-gap quantum spin Hall insulator: electronic structures and transport properties

Meimei Wu[1,2], Chenqiang Hua[1], Biyu Song[1,3], Guo-Xiang Zhi[2], Tianchao Niu[1,2] and Miao Zhou[1,2,3,*]

[1] Institute of International Innovation, Beihang University, Hangzhou 311115, People's Republic of China
[2] Tianmushan Laboratory, Hangzhou 310023, People's Republic of China
[3] School of Physics, Beihang University, Beijing 100191, People's Republic of China
[*] Author to whom any correspondence should be addressed.

E-mail: mzhou@buaa.edu.cn

Keywords: quantum spin Hall insulator, nanoribbons, semiconductor substrate, epitaxial growth, electronic structure, quantum transport

Supplementary material for this article is available online

Abstract

Two-dimensional Bi grown on semiconductor substrate, a large-gap quantum spin Hall insulator characterized by a (p_x, p_y)-orbital hexagonal lattice, has been theoretically proposed and experimentally confirmed. Here, by combining tight-binding modeling with first-principles calculations, we investigate the electronic structures and quantum transport properties of Bi nanoribbons (NRs), focusing on the topological edge states for nanoelectronics. We reveal that band gap emerges due to the quantum confinement, and the gaps size depends crucially on the width and edge shape: for zigzag NRs, the gap decreases monotonically with the increase of width; while for armchair NRs, it can be categorized into three subgroups with band-gap hierarchies of $E_{g(3p-1)} > E_{g(3p)} > E_{g(3p+1)}$, so that the overall relation is an oscillating dependence dumped by 1/width decay. Quantum transport calculations demonstrate that the conductance is quantized to $2e^2/h$, and an applied gate voltage can efficiently regulate the conductance plateau, originating from the interplay between gate voltage and topological gaps. Furthermore, the quantized conductance remains robust against strong disorder, suggesting the unique advantage of topological states for electronic transport. This work not only provides fundamental insights into the electronic properties of topological insulator nanostructures, but also sheds light on the potential applications of exotic states for quantum devices compatible with semiconductor technology.

1. Introduction

As a new state of quantum matter, topological insulators (TIs) have attracted tremendous interest in condensed matter and materials physics communities in the past years. They possess time-reversal-symmetry protected conducting surface/edge states residing inside an insulating bulk gap, implying significant implications in dissipationless transport and quantum computing devices [1, 2]. In particular, two-dimensional (2D) TIs, also known as quantum spin Hall (QSH) insulators, possess one-dimensional (1D) helical edge states at the boundary, which are more robust against non-magnetic disorder compared to the surface states in three-dimensional TIs because the only backscattering channel is forbidden [3–7]. Graphene is the first model system that was theoretically predicted to exhibit QSH effect (Kane and Mele) [8]. However, with the weak spin–orbit coupling (SOC) strength in carbon, it is difficult to detect the topological edge states due to the negligible topological gap [9–11]. Thus far, plenty of QSH insulators have been explored from both theoretical and experimental sides, including but not limited to, semiconductor quantum wells [12, 13], monoelemental structures beyond graphene [14–16], metal dichalcogenides [17–20], metal-organic frameworks [21–23] and recently jacutingaite [24–26]. Despite these studies, successful

preparation and characterization of QSH insulators are rare [18, 27–29]. It is highly desirable to fabricate QSH insulators with a sizable bulk gap, a critical requirement for room-temperature implementation.

In this endeavor, Zhou *et al* previously proposed to achieve QSH insulators by epitaxially growing heavy elements (such as Bi) on semiconductor substrate [30]. Through an intriguing 'substrate-orbital-filtering' effect, the grown Bi layer is featured by a 2D (p_x, p_y)-orbital hexagonal lattice model [31–34], whose effective SOC arises from the on-site spin–orbit interaction, so that the SOC strength is much enhanced compared to that of graphene, leading to an extremely large topological gap of ~0.8 eV. Interestingly, this was later experimentally confirmed by Reis *et al* [35], who used scanning tunneling microscopy/spectroscopy (STM/STS) and angle-resolved photoemission spectroscopy to clearly characterize the large topological gap and conductive edge states. Formation of exotic quantum phase on semiconductor surface is of paramount importance, as it not only exhibits intrinsic compatibility with current semiconductor technology, but also allows facile manipulation of the topological states with high tunability and fidelity for practical applications, such as in novel electronics/spintronics and fault-tolerant quantum computation.

Here, by using the experimentally grown of Bi on SiC(0001) substrate (Bi/SiC) as a prototype probe, we investigate the electronic structures and transport properties of large-gap QSH insulator nanoribbons (NRs), with special attention paid to the topological edge states for nanoelectronics. 1D NRs, combining flexibility, unidirectional properties, high surface area and tunable edge effects, have been extensively studied in graphene [36–45], MoS_2 [46, 47], phosphorene [48, 49], among many other 2D structures [50–53]. For Bi/SiC, it is essential to construct Bi NRs so that the helical edge states can be utilized in a controlled way. In experiment, this could be achieved by precisely patterning the epitaxially grown Bi layer on semiconductor surface [54, 55] or by direct templated growth [56]. By joint first-principles and tight-binding (TB) approaches, we are able to extract the key parameters that describe the band structures of Bi/SiC, so that the electronic properties of Bi NRs with different ribbon width (N) and edge shapes (zigzag or armchair) can be explored in a systematic way. While semi-infinite Bi NRs on SiC has gapless edge states connecting the upper and lower bulk band edges to form a 1D Dirac cone [30, 32, 33, 57, 58], our calculations show that NRs with limited width exhibit a finite band gap, and the gap size (E_g) is strongly enhanced by quantum confinement. Specifically, for zigzag NRs, E_g decreases monotonically with width; while for armchair NRs, E_g can be divided into three subfamilies depending on $N = 3p - 1$, $3p$ or $3p + 1$ (where p is an integer), with each subfamily scaling inversely with N. Surprisingly, for armchair NRs with the same p, E_g follows $E_{g(3p-1)} > E_{g(3p)} > E_{g(3p+1)}$, which is in sharp contrast with the case of armchair graphene NRs (GNRs) [39–43]. For transport properties, Canonico *et al* [59] performed spin and charge transport calculations on 2D Bi/SiC recently, demonstrating the interplay between topology, disorder, valley and spin degrees of freedom. In this work, we consider a two-terminal device with Bi NRs and reveal that the conductance is quantized to $2e^2/h$ due to the doubly degenerate edge states. Meanwhile, an applied gate voltage can efficiently regulate the conductance plateau according to the alignment between the gate voltage and topological gap. The fundamental mechanisms underlying the obtained results are discussed. As the quantum conductance is robust against strong disorder, our results suggest the great promise of QSH insulator NRs for dissipationless interconnects.

2. Methods

2.1. First-principles calculations

First-principles calculations based on density functional theory (DFT) were performed with the projector-augmented wave method as implemented in the Vienna *ab initio* simulation package [60, 61]. The plane-wave energy cutoff was set to 400 eV. The generalized gradient approximation with the Perdew–Burke–Ernzerhof formalism [62] was used for the exchanged-correlation functional. As standard DFT usually underestimates the band gap of semiconductors, we have employed the more sophiscated Heyd–Scuseria–Ernzerhof hybrid functional for electronic structure calculations [63]. SOC was treated as a perturbation term [64]. The SiC substrate is modelled by hydrogenated SiC(0001) surface using a slab of sixteen atomic layers, where both the top Si atoms and the bottom C atoms are terminated with H. For Bi/SiC, Bi atoms are placed on the top Si atoms with H removed in a way that a hexagonal Bi lattice is formed. During structural optimization, the bottom ten layers were fixed while all other atoms were fully relaxed until the atomic forces were smaller than 0.01 eV Å^{-1}. The vacuum region in the direction normal to surface was set to 30 Å to eliminate the interaction between neighboring slabs. The Brillouin zone was sampled by a $15 \times 15 \times 1$ Γ-centered k-point mesh. The lattice constant of Bi hexagonal lattice is 5.35 Å, corresponding to a $(\sqrt{3} \times \sqrt{3})R30°$ superstructure of the 4H-SiC(0001) surface.

2.2. TB modeling

As the electronic structure of Bi/SiC can be described by a simplified TB model of 2D hexagonal lattice with (p_x, p_y) orbitals, we constructed the effective Hamiltonian as expressed by [30, 31],

$$\mathcal{H} = t_{\parallel} \sum_{\vec{r}\in A,s,i=1\sim3} \mathrm{p}^{\dagger}_{\vec{r},i,s,\sigma}\mathrm{p}_{\vec{r}+a\hat{e}_i,i,s,\sigma} + t_{\perp} \sum_{\vec{r}\in A,s,i=1\sim3} \mathrm{p}^{\dagger}_{\vec{r},i,s,\pi}\mathrm{p}_{\vec{r}+a\hat{e}_i,i,s,\pi} + i\lambda_I \sum_{\vec{r},s} \sigma^z_{ss}\mathrm{p}^{\dagger}_{\vec{r},x,s}\mathrm{p}_{\vec{r},y,s} + i\lambda_R \sum_{\vec{r}\in A,s,i=1\sim3} \mathrm{p}^{\dagger}_{\vec{r},x,\bar{s}}[\hat{z}\cdot(\hat{\sigma}\times\hat{e}_i)]_{\bar{s}s}\mathrm{p}_{\vec{r}+a\hat{e}_i,y,s} + h.c., \quad (1)$$

where $t_{\parallel}$ ($t_{\perp}$) denotes σ- (π-)bonding that can be parametrized from the standard Slater–Koster formalism [65], and λ_I (λ_R) represents intrinsic (Rashba) SOC strength. $s = \uparrow/\downarrow$ denotes one of the two spin states. a is the nearest neighbor bond length. $\hat{e}_1 = \frac{1}{2}\hat{e}_x + \frac{\sqrt{3}}{2}\hat{e}_y$, $\hat{e}_2 = -\frac{1}{2}\hat{e}_x + \frac{\sqrt{3}}{2}\hat{e}_y$, $\hat{e}_3 = -\hat{e}_y$ are three unit vectors from sublattice A to its three neighbors in sublattice B. $p_{\vec{r},i,\sigma} \equiv (p_{\vec{r},x}\hat{e}_x + p_{\vec{r},y}\hat{e}_y)\cdot\hat{e}_i$ and $p_{\vec{r},i,\pi} \equiv (-p_{\vec{r},x}\hat{e}_y + p_{\vec{r},y}\hat{e}_x)\cdot\hat{e}_i$ ($i = 1, 2, 3$) are the projections of the p orbitals parallel and perpendicular to the bonding direction $\hat{e}_i$. a is the nearest neighbor bond length. σ^z_{ss} are the diagonal elements of Pauli matrix σ_z. $h.c.$ is the Hermitian conjugate. $\hat{\sigma}$ symbolizes the Pauli vector. $\bar{s}$ has the opposite spin direction specified by s.

3. Electronic structures

Figure 1(a) shows the optimized structure of Bi epitaxially grown on SiC(0001) surface, where the planar Bi layer forms a 2D hexagonal lattice and is stabilized on the substrate, as clearly observed by STM image [35]. Strong hybridization of Bi p_z orbital with the electronic states of underlying substrate leads to an 'substrate-orbital-filtering' effect [30], so that only the (p_x, p_y) orbitals of Bi are left on each site on the hexagonal pattern, as illustrated in figure 1(b). This (p_x, p_y)-orbital hexagonal lattice model typically produces four bands, with two Dirac bands forming a Dirac point at K and two flat bands that touch the Dirac bands at Γ forming two quadratic points. Inclusion of SOC opens a central gap at the Dirac point and two lateral gaps at the quadratic points, which are all topologically nontrivial [30, 32]. We calculated the band structure of Bi/SiC by DFT, and indeed found that SOC opens a large energy gap within the bulk gap of SiC (figure 1(c)). By fitting the low-energy characteristics of band structure using the TB Hamiltonian (equation (1)), we can obtain the key TB parameters that describe four-band model within a (p_x, p_y)-orbital hexagonal lattice, i.e. $t_{\parallel} = 1.953$ eV, $t_{\perp} = -0.205$ eV, $\lambda_I = 0.435$ eV, and $\lambda_R = 0.032$ eV. These parameters are generally in agreement with previous reports [59, 66].

Then, we turn to investigate the physical properties of Bi NRs. When shaped into 1D NRs on SiC substrate, Bi may exhibit either zigzag or armchair edges, as shown in figure 2(a). Following the previous convention of GNRs [37, 38], zigzag NRs are denoted by the number of zigzag chains (N_Z) across the ribbon width, while armchair NRs are denoted by the number of dimer lines (N_A) across the ribbon width. We studied the stability of the supported Bi NRs through the formation energy (E_F), as defined by, $E_F = [E_{Bi/SiC} - (E_{SiC} + n \times E_{Bi})]/n$, where $E_{Bi/SiC}$, E_{SiC} and E_{Bi} represent the total energy of Bi ribbon supported on SiC(0001) substrate, the energy of pure SiC and a single Bi atom, respectively. n is the number of Bi atoms in the system. The calculated formation energies for zigzag and armchair Bi NRs of different width are listed in table S1 in supplementary material. It was found that the formation energies are around -4.9 eV, larger than the cohesive energy of Bi in the bulk form [67]. To explore the thermal stability, we performed *ab initio* molecular dynamics simulations at 300 K for 20 ps with a time step of 2 fs using the canonical ensemble and the Nosé–Hoover thermostat [68, 69]. The corresponding fluctuations of energy with time are shown in figure S1 (supplementary material). Our stability analysis demonstrates that Bi NRs are intrinsically stable on the substrate, indicating high probability of obtaining 1D Bi nanostructures via high-resolution patterning or templated growth [54–56].

We computed the band structures of both zigzag and armchair NRs with a series of width ($N_Z = 2 \sim 21$, $N_A = 3 \sim 31$). Here, the electronic properties of Bi NRs are calculated by TB method, with the TB parameters obtained by fitting the DFT results as presented above. It was found that topological edge states appear in both the central gap and the two lateral gaps. Interestingly, a noticeable energy gap (E_g) is opened between the edge states in the central gap region, which depends on the edge shape and ribbon width. We summarize the obtained variations of E_g against ribbon width in figures 2(b) and (c). For zigzag edge, the smallest ribbon ($N_Z = 2$) has a gap of 0.36 eV. With increased N_Z, the gap size drops dramatically and becomes almost zero (~0.001 eV) when $N_Z = 7$ (figure 2(b)). For armchair edge, we found that the band structures can be classified into three subgroups with $N_A = 3p - 1$, $3p$, and $3p + 1$, so that E_g has an oscillating dependence on the ribbon width. With the same p, the gap size follows $E_{g(3p-1)} > E_{g(3p)} > E_{g(3p+1)} (\neq 0)$.

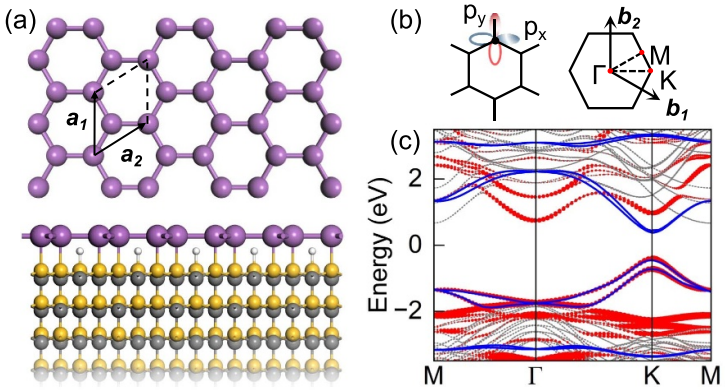

Figure 1. (a) Optimized structure of Bi grown on SiC(0001) substrate, forming a 2D hexagonal lattice with $(\sqrt{3} \times \sqrt{3})$ R30° commensurate registry. ($\mathbf{a}_1$, $\mathbf{a}_2$) denotes the unit cell. The purple, yellow, grey and white balls represent Bi, Si, C and H atoms, respectively. (b) Schematic illustration of a (p_x, p_y)-orbital hexagonal lattice and the Brillouin zone with reciprocal lattice ($\mathbf{b}_1$, $\mathbf{b}_2$) and high-symmetry points labeled. (c) Fitting of DFT band structures by TB modeling (blue curves). The size of red dots indicates the relative contribution of Bi (p_x, p_y) orbitals obtained by DFT.

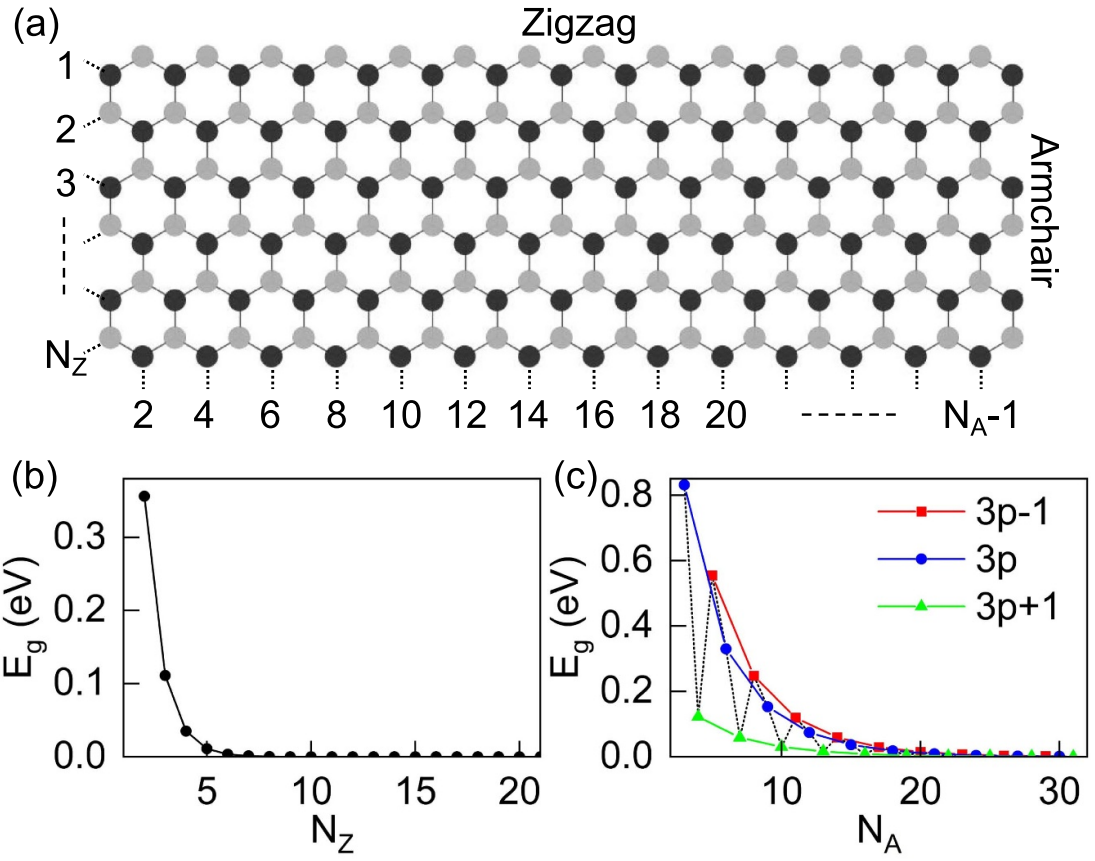

Figure 2. (a) Structure of Bi NRs, in which top and bottom are zigzag edges, and left and right are armchair edges. The width of NRs with zigzag (N_Z) and armchair (N_A) edges are indicated. Variations of the calculated band gap (E_g) as a function of ribbon width with zigzag (b) and armchair (c) edges.

The smallest armchair ribbon ($N_A = 3$) has the largest E_g of 0.83 eV, which drops to 0.12 eV for the ribbon with $N_A = 4$ and climbs to 0.55 eV when $N_A = 5$. With $N_A = 25$, E_g reduces to ~0.001 eV. As such, Bi NRs approach the bulk limit when the ribbon width reaches 29.3 Å (64.2 Å) for zigzag (armchair) type.

In figure 3, we plot out the band structures of Bi NRs with selected ribbon width. For zigzag NRs (figures 3(a)–(d)), E_g is 0.04 eV for $N_Z = 4$, which reduces to 0.01 eV with $N_Z = 5$ and 0.004 eV with $N_Z = 6$. For $N_Z = 7$ or larger NRs, the band structure can be regarded as that of semi-finite NRs with gapless edge states. For armchair NRs (figures 3(e)–(h)), the gap size for $N_A = 7$ is 0.06 eV, which greatly increases to

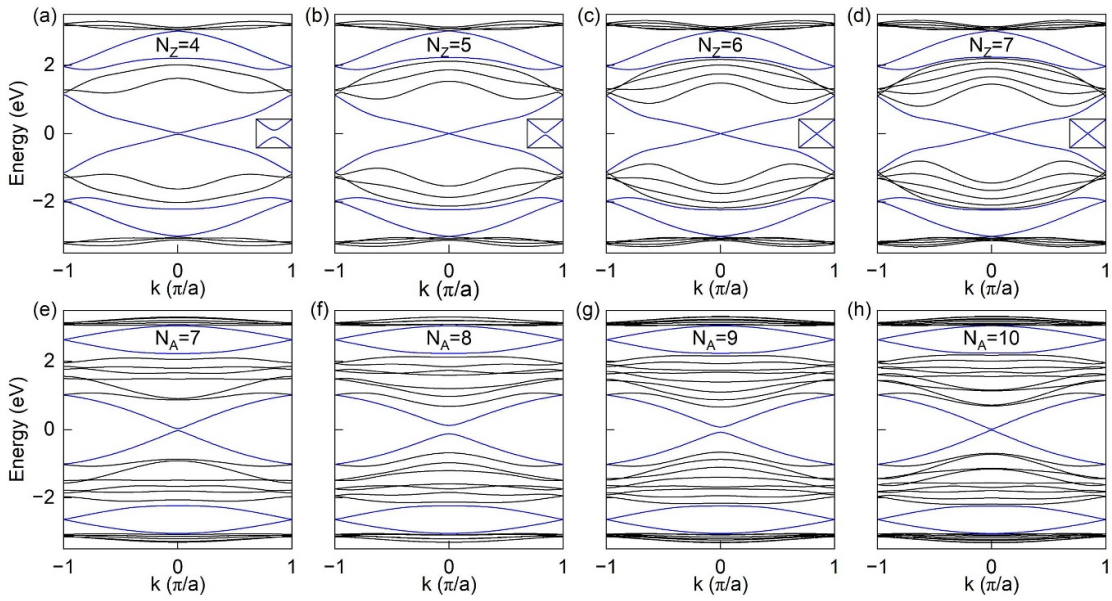

Figure 3. (a)–(d) Band structures of zigzag Bi NRs with $N_Z = 4, 5, 6$, and 7. (e)–(h) Band structures of armchair Bi NRs with $N_A = 7, 8, 9$, and 10. Black curves represent the bulk states and blue curves indicate the edge states. Insets in (a)–(d) show the enlarged views of edge bands within an energy range of $-0.07 \sim 0.07$ eV, highlighting the width-dependent energy gap.

0.25 eV with $N_A = 8$. Further increase of width decreases E_g to 0.15 eV (0.03 eV) with $N_A = 9$ ($N_A = 10$), following the band hierarchies of $E_{g(3p-1)} > E_{g(3p)} > E_{g(3p+1)}$ strictly. It should be noted that during the calculations of NRs, the Rashba SOC was neglected because λ_R is one order of magnitude smaller than λ_I, which does not change the overall topological order of the system.

As discussed before, Bi NRs with semi-infinite width have a pair of Dirac-cone-like edge states with diminished energy gap. However, when shaped into NRs with finite width, band gap emerges due to the non-negligible interaction between edge states at the two sides. In particular, E_g decreases monotonically with width for zigzag NRs, while it has an oscillating dependence dumped by 1/width decay for armchair NRs. Such behaviors remind us of the electronic properties of GNRs. In literature, it was reported that GNRs with zigzag shaped edges have band gaps due to spin ordered states at the two edges [36], and the gap size decreases with increasing width [39–43]. Here, we have also considered zigzag Bi NRs with different ferromagnetic and antiferromagnetic configurations (see figure S2 in supplementary material), and found that they all converge to the non-magnetic state. Therefore, the band gap existed in zigzag Bi NRs originates from quantum confinement effect, so that the gap size shrinks rapidly with width. For GNRs with armchair edges, earlier TB simulations showed either metallic or semiconducting properties with $E_{g(3p)} \gtrsim E_{g(3p+1)} > E_{(3p+2)} (= 0)$ [39–41], while subsequent first-principles calculations suggested that no metallic GNRs exist and the gaps can be classified into three different categories with $E_{g(3p+1)} > E_{g(3p)} > E_{g(3p+2)} (\neq 0)$ [39], resulting from the crucial effects of edges. The electronic structures of armchair GNRs have been broadly discussed in literature, and it was shown that the three categories have unique aromatic, electronic and topological properties, which are related to the inherent shell structure of graphene and geometrical/topological constraints [44, 45]. This scenario is in sharp contrast with the size hierarchy of $E_{g(3p-1)} > E_{g(3p)} > E_{g(3p+1)} (\neq 0)$ for armchair Bi NRs as revealed here. The difference should be ascribed to the fundamental model associated with quantum confinement: as graphene can be described by a single-orbital (p_z) hexagonal lattice with a two-band model, while Bi/SiC is featured by a (p_x, p_y)-orbital hexagonal lattice model with four bands, the relative strength of σ and π bonding is drastically different, thus contributing to the different band-gap hierarchies when edges are present.

To shed light on the influence of σ and π bonding on the band structures of Bi NRs, we artificially excluded the π bonding parameter ($t_\perp$) and only considered the hopping integral of σ bonding ($t_\parallel$), because the amplitude of π bonding (0.205 eV) is much smaller than that of σ bonding (1.953 eV). The calculated band gaps as a function of ribbon width are presented in figures S3 and S4 of supplementary material. It was found that E_g for zigzag NRs follows a similar decreasing fashion with width (comparing figure S4 with figure 2(b)), while for armchair NRs, the band gap becomes zero when $N_A = 3p + 1$, thus transforming the structures from semiconducting to metallic systems (see figure S3 in supplementary material). This indicates the crucial role of π bonding in determining the electronic properties of Bi NRs. Furthermore, we explored the SOC effects on the electronic structures (to simulate elements with different SOC grown on the substrate,

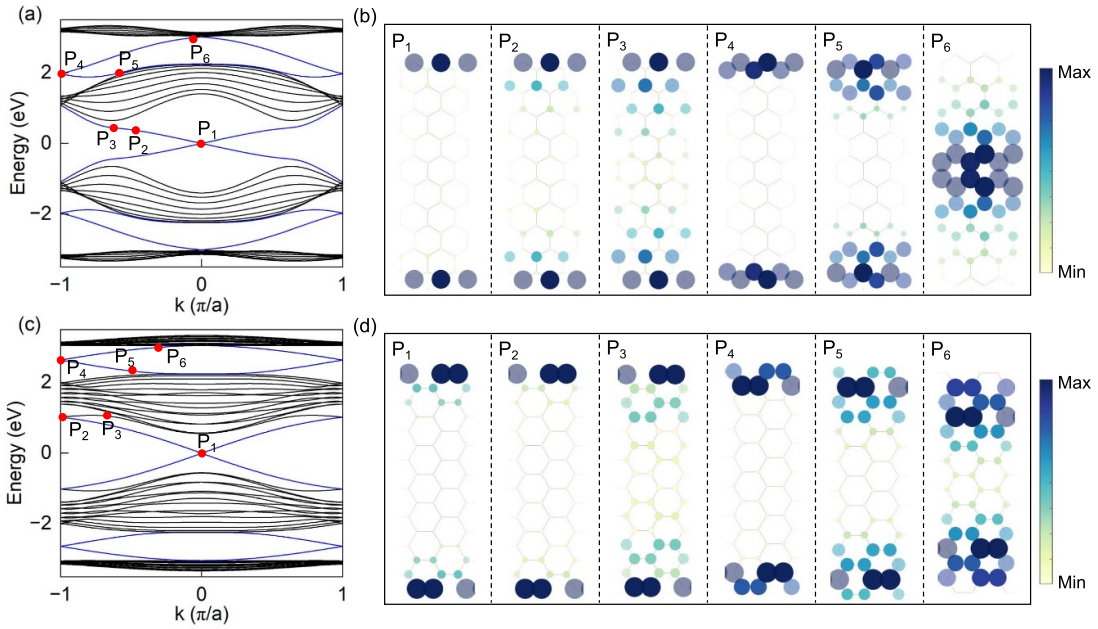

Figure 4. (a) Band structure of a zigzag Bi ribbon with $N_Z = 10$. The selected points along edge bands are indicated. (b) Real-space charge density distributions for the points shown in (a). The amplitude of states is proportional to the radius and color. (c) Band structure of an armchair Bi ribbon with $N_A = 16$. (d) Real-space charge density distributions corresponding to (c).

such as Pb, Sb, Sn, Ga, In and Tl [33]), and found that the trends of band-gap evolution with respect to ribbon width are maintained, though the detailed gap size is modified (figures S5 and S6).

To directly see the topological edge states in Bi NRs, we plot out the charge density distributions in real space. Figure 4(a) presents the band structure of a zigzag ribbon ($N_Z = 10$), where several typical points along the edge bands are selected within the central gap (P_1, P_2 and P_3) and the lateral gap (P_4, P_5 and P_6). The corresponding spatial charge densities are shown in figure 4(b). Clearly, P_1 and P_4, which are far away from bulk states, have charge density strongly localized in the edge region. For P_2, P_4 and P_5 that are closer to the bulk bands, the density becomes delocalized and extends into the bulk region. For P_6, with energy overlapping with bulk bands, the charge density is mainly spread over the central region of ribbon. Therefore, the edge states away from bulk bands tend to be more localized, which should be more immune to bulk imperfections. We also performed analyses on an armchair ribbon ($N_A = 16$), where similar behaviors can be observed (figures 4(c) and (d)).

4. Transport properties

As the topological states in Bi/SiC is intrinsically integrated in a semiconductor substrate, it is highly desired to utilize these states for carrier transport. Here, we constructed a field-effect transistor (FET) device to explore the transport properties. As shown in figure 5(a), the model device consists of two electrodes (source and drain) and a central scattering region. When electrons travel through this device, the conductance G can be calculated by Landauer formula [70],

$$G = \frac{2e^2}{h} \sum_{i \in s, j \in d} |S_{ij}|^2, \tag{2}$$

where s and d denote the source and drain electrodes of the device, and S_{ij} is the scattering matrix from an incoming propagating mode i to an outgoing mode j. Here, the scattering matrix formalism is used, as it is equivalent to the nonequilibrium Green's function approach based on the Fisher-Lee relation [71], but has a simpler structure and is more stable in computations. In this work, we used KWANT to perform the quantum transport calculations [72].

In the model device, a top gate is added to control the conductance between source and drain, which is electrostatically coupled through a thin dielectric layer (figure 5(a)). Physically, when a gate voltage (V_g) is applied in the scattering region, the chemical potential is changed and the band structure of scattering region will be shifted in energy (figure 5(b)). Depending on the matching between the central/lateral topological gaps of the electrode and those of the scattering region, quantized conductance could be efficiently tuned.

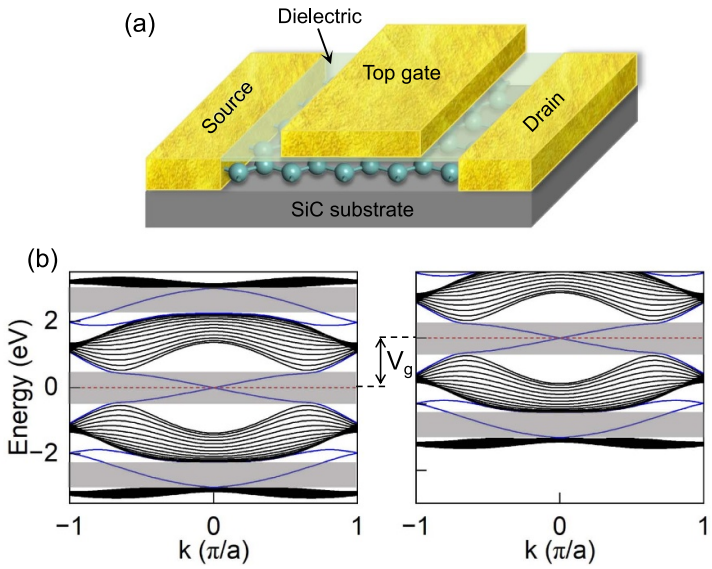

Figure 5. (a) Schematic of a FET device based on Bi/SiC. (b) Band structure of a zigzag Bi ribbon ($N_Z = 16$) as an electrode (left panel) and as a scattering region with an applied gate voltage V_g (right panel). The topological gaps are highlighted by gray shadow.

For instance, conductance plateaus will appear when an electron with an energy of $-\Delta/2 < E < \Delta/2$ (Δ is the size of the central gap) passes through the edge-state channels (in either the central gap or the two lateral gaps). Otherwise, the electron will experience multiple scattering with bulk states and the quantized conductance could disappear.

Figure 6 shows the calculated conductance spectra of the device based on a zigzag Bi ribbon. The ribbon has a width of $N_Z = 16$, so it is a QSH insulator with metallic gapless edge states. The central scattering region includes 30 dimer lines, which is long enough to comprise all the perturbations on the system due to the presence of scatters [73]. Without gate voltage ($V_g = 0$), three conductance plateaus with $2e^2/h$ can be clearly observed in the energy ranges of $-3.02 \sim -2.25$, $-0.54 \sim 0.54$ and $2.25 \sim 3.02$ eV, denoted as region I, II and III respectively. The quantized conductance $2e^2/h$ originates from electron transport through two edge-state channels within one ribbon, and the three plateaus correspond to the three topological gaps. The conductance can reach its maximum value allowed by the number of bulk channels in the electrodes. We considered the effect of Rashba SOC ($\lambda_R = 0.032$ eV) on the transport properties, and found that the conductance shows little variation with the inclusion of λ_R (figure S7). With an applied gate voltage ($V_g = 0.3$ V), the maximum conductance decreases significantly due to the mismatch of bulk channels between electrodes and scattering region. Meanwhile, the three quantized plateaus could still be observed. With an increased gate voltage ($V_g = 0.8$ V), the three plateaus seem to be up-shifted in energy. By examining the correspondence between band structures (figure 5(b)) and conductance spectra (figure 6), we can find several interesting behaviors: first, the plateaus contributed by the electron transport from the edge states of electrode to the edge-state channels of scattering region shrinks with increased gate voltages, which could be understood by the reduced overlap of the edge states. Second, for electron transport from the bulk states of electrode to the edge-state channels of scattering region, the conductance is quantized, as determined by the two edge-state channels. Third, for electron transport through the bulk-state channels of scattering region, multiple scattering of the electrons with interband transition occurs, leading to a complicated behavior of conductance with strong fluctuation.

Increase of the gate voltage to 1.7 V results in shortened quantized plateaus. Meanwhile, the plateau in region I disappears as there is no conducting channel in the potential barrier region with no electron transmission. When the gate voltage is 4.5 V or higher, a small quantized plateau can be observed in region III. This plateau will be destroyed when V_g reaches 6.0 V. We also explored the transport properties of the FET device based on armchair Bi NRs, and the conductance spectra are presented in figures S8 and S9. Our results demonstrate that the quantized conductance of Bi NRs can be effectively regulated through gate voltage, suggesting the great potential of Bi/SiC for electronic devices.

In practice, substrate supported 2D structures are subject to various types of defects during material synthesis or device setting, which could affect the operating performance of nanoelectronic devices. Hence, we further considered the disorder effect and simulated its influence on the conductance. To achieve this, an on-site potential ϵ_i is introduced in the central scattering region that is randomly distributed within $[-W/2,$

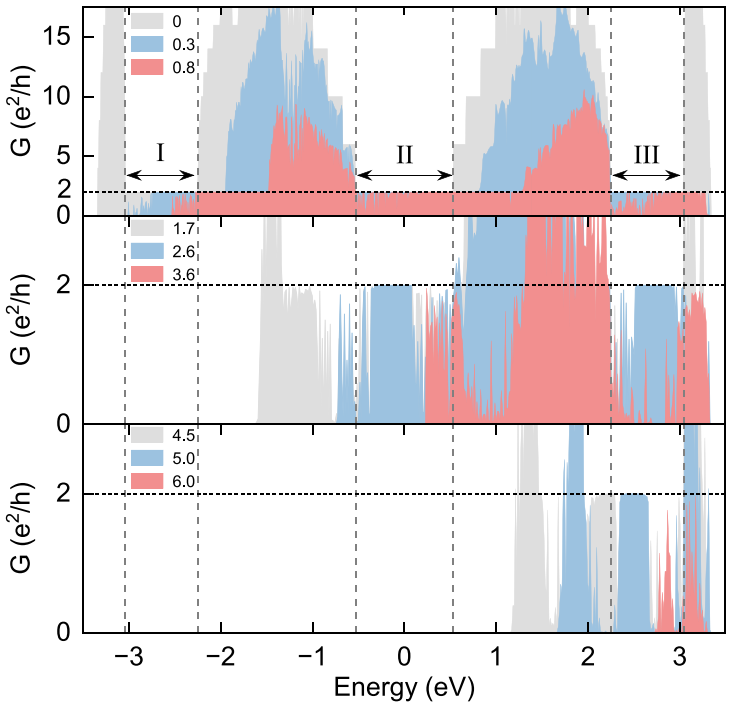

Figure 6. Conductance spectra of a FET device based on a zigzag Bi ribbon ($N_Z = 16$). Different gate voltages are applied, with $V_g = 0$, 0.3, 0.8, 1.7, 2.6, 3.6, 4.5, 5.0, and 6.0 V. The quantized plateaus ($2e^2/h$) are indicated by dashed lines.

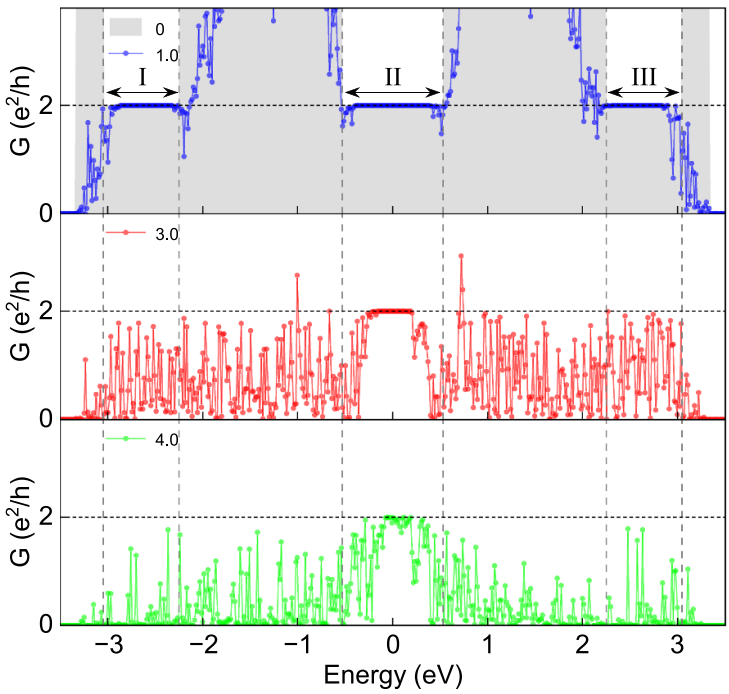

Figure 7. Conductance spectra of the FET device with different magnitudes of disorder strength ($W = 0$, 1.0, 3.0, and 4.0 eV). The quantized plateaus are indicated.

$W/2$], where W denotes the disorder strength. The calculated conductance spectra with different disorder strength W are shown in figure 7. Obviously, the maximum conductance contributed by bulk states decreases significantly with increasing W, while the quantized conductance plateaus are more robust against disorders. In particular, with $W = 1.0$ eV, all the three conductance plateaus are present with little impact from disorders. With increased W (3.0 eV), the conductance plateaus in regions I and III (the two lateral gaps) disappear, while the conductance plateau in region II (the central gap) still exists. When W reaches 4.0 eV, which is twice as large as $t_{||}$, the conductance spectrum is strongly perturbed but the central plateau

could still be detected. The different responses of conductance plateaus in the central and two lateral regions lie in the distinguished properties of the electronic states around these gaps: the central gap is opened between two Dirac bands described by a massless Dirac equation, while the two lateral gaps are split between two quadratic points with parabolic bands characterized by Schrödinger equation [74]. Nevertheless, our findings suggest the unique advantage of topological edge states for electronic transport, which are robust against strong disorders (More results on the FET device with armchair NRs are presented in figure S10 in supplementary material). Meanwhile, as the topological states of Bi NRs are intrinsically integrated into SiC, and the large topological gap ensures room-temperature applications, the present system should provide a promising platform for the implementation of exotic states for quantum devices compatible with current mature technology.

5. Conclusion

In summary, by combining first-principles and TB simulations, we have systematically investigated the electronic structures and transport properties of Bi NRs on SiC substrate, aiming to understand the topological edge states for electronic devices. We show that band gap emerges between edge states due to quantum confinement, and the gap size depends crucially on the width and edge shape of NRs. In particular, for zigzag NRs the gap decreases monotonically with increasing width, while for armchair NRs it can be categorized into three subfamilies with each subfamily decaying with 1/width. Quantum transport calculations reveal the quantized conductance that are robust against strong disorder. Meanwhile, the conductance plateau can be readily tuned by an applied gate voltage. The physical mechanisms underlying the obtained findings are discussed. We expect this study to stimulate interest among experimentalists in synthesizing novel quantum materials and devices for room-temperature applications, such as in nanoelectronic/spintronic and quantum computing devices.

Data availability statement

All data that support the findings of this study are included within the article (and any supplementary files).

Acknowledgments

This work is supported by the Natural Science Foundation of Zhejiang Province (LZ22A040004 and LQ23A040023), the National Key R&D Program of China (2022YFF0708800), the National Natural Science Foundation of China (11674042) and the Fundamental Research Funds of the Central Universities. We also acknowledge the support from the High-performance Computing Centre of Institute of International Innovation, Beihang University.

ORCID iD

Miao Zhou https://orcid.org/0000-0003-1390-372X

References

[1] Hasan M Z and Kane C L 2010 *Rev. Mod. Phys.* **82** 3045
[2] Qi X-L and Zhang S-C 2011 *Rev. Mod. Phys.* **83** 1057
[3] Kane C L and Mele E J 2005 *Phys. Rev. Lett.* **95** 146802
[4] Xu C and Moore J E 2006 *Phys. Rev.* B **73** 045322
[5] Ni X, Huang H and Liu F 2020 *Phys. Rev.* B **101** 125114
[6] Stühler R, Kowalewski A, Reis F, Jungblut D, Dominguez F, Scharf B, Li G, Schäfer J, Hankiewicz E M and Claessen R 2022 *Nat. Commun.* **13** 3480
[7] Stühler R, Reis F, Müller T, Helbig T, Schwemmer T, Thomale R, Schäfer J and Claessen R 2020 *Nat. Phys.* **16** 47
[8] Kane C L and Mele E J 2005 *Phys. Rev. Lett.* **95** 226801
[9] Bao C *et al* 2021 *Phys. Rev. Lett.* **126** 206804
[10] Weeks C, Hu J, Alicea J, Franz M and Wu R 2011 *Phys. Rev.* X **1** 021001
[11] Qiao Z, Ren W, Chen H, Bellaiche L, Zhang Z, MacDonald A H and Niu Q 2014 *Phys. Rev. Lett.* **112** 116404
[12] Bernevig B A, Hughes T L and Zhang S-C 2006 *Science* **314** 1757–61
[13] König M, Wiedmann S, Brüne C, Roth A, Buhmann H, Molenkamp L W, Qi X-L and Zhang S-C 2007 *Science* **318** 766–70
[14] Liu C-C, Feng W and Yao Y 2011 *Phys. Rev. Lett.* **107** 076802
[15] Yu X-L, Huang L and Wu J 2017 *Phys. Rev.* B **95** 125113
[16] Xu Y, Tang P and Zhang S-C 2015 *Phys. Rev.* B **92** 081112
[17] Qian X, Liu J, Fu L and Li J 2014 *Science* **346** 1344–7
[18] Wu S, Fatemi V, Gibson Q D, Watanabe K, Taniguchi T, Cava R J and Jarillo-Herrero P 2018 *Science* **359** 76–79
[19] Ma Y, Kou L, Li X, Dai Y, Smith S C and Heine T 2015 *Phys. Rev.* B **92** 085427

[20] Ma F, Gao G, Jiao Y, Gu Y, Bilic A, Zhang H, Chen Z and Du A 2016 *Nanoscale* **8** 4969–75
[21] Wang Z F, Liu Z and Liu F 2013 *Nat. Commun.* **4** 1471–5
[22] Wang Z F, Su N and Liu F 2013 *Nano Lett.* **13** 2842
[23] Liu Z, Wang Z-F, Mei J-W, Wu Y-S and Liu F 2013 *Phys. Rev. Lett.* **110** 106804
[24] Kandrai K *et al* 2020 *Nano Lett.* **20** 5207–13
[25] Pei C *et al* 2021 *npj Quantum Mater.* **6** 98
[26] Luo F, Hao X, Jia Y, Yao J, Meng Q, Zhai S, Wu J, Dou W and Zhou M 2021 *Nanoscale* **13** 2527–33
[27] Deng J *et al* 2018 *Nat. Mater.* **17** 1081–6
[28] Tang S *et al* 2017 *Nat. Phys.* **13** 683–7
[29] Bampoulis P, Castenmiller C, Klaassen D J, van Mil J, Liu Y, Liu C-C, Yao Y, Ezawa M, Rudenko A N and Zandvliet H J W 2023 *Phys. Rev. Lett.* **130** 196401
[30] Zhou M, Ming W, Liu Z, Wang Z, Li P and Liu F 2014 *Proc. Natl Acad. Sci. USA* **111** 14378–81
[31] Wu C, Bergman D, Balents L and Sarma S D 2007 *Phys. Rev. Lett.* **99** 070401
[32] Zhang G-F, Li Y and Wu C 2014 *Phys. Rev.* B **90** 075114
[33] Zhou M, Ming W, Liu Z, Wang Z, Yao Y and Liu F 2014 *Sci. Rep.* **4** 7102
[34] Yao J, Hao X, Song B, Jia Y, Hua C and Zhou M 2022 *Nano Futures* **6** 021001
[35] Reis F, Li G, Dudy L, Bauernfeind M, Glass S, Hanke W, Thomale R, Schäfer J and Claessen R 2017 *Science* **357** 287–90
[36] Brey L and Fertig H A 2006 *Phys. Rev.* B **73** 235411
[37] Wakabayashi K, Fujita M, Ajiki H and Sigrist M 1999 *Phys. Rev.* B **59** 8271
[38] Son Y-W, Cohen M L and Louie S G 2006 *Nature* **444** 347–9
[39] Son Y-W, Cohen M L and Louie S G 2006 *Phys. Rev. Lett.* **97** 216803
[40] Nakada K, Fujita M, Dresselhaus G and Dresselhaus M S 1996 *Phys. Rev.* B **54** 17954–61
[41] Yang L, Park C-H, Son Y-W, Cohen M L and Louie S G 2007 *Phys. Rev. Lett.* **99** 186801
[42] Liu W, Wang Z F, Shi Q W, Yang J and Liu F 2009 *Phys. Rev.* B **80** 233405
[43] Zheng H, Wang Z F, Luo T, Shi Q W and Chen J 2007 *Phys. Rev.* B **75** 165414
[44] Zdetsis A D 2020 *J. Phys. Chem.* C **124** 7578–84
[45] Zdetsis A D 2022 *Phys. Chem. Chem. Phys.* **24** 10334
[46] Rostami H, Asgari R and Guinea F 2016 *J. Phys.: Condens. Matter* **28** 495001
[47] Davelou D, Kopidakis G, Kaxiras E and Remediakis I N 2017 *Phys. Rev.* B **96** 165436
[48] Tran V and Yang L 2014 *Phys. Rev.* B **89** 245407
[49] Wu Q, Shen L, Yang M, Cai Y, Huang Z and Feng Y P 2015 *Phys. Rev.* B **92** 035436
[50] Ding Y, Wang Y and Ni J 2009 *Appl. Phys. Lett.* **94** 073111
[51] Matthes L and Bechstedt F 2014 *Phys. Rev.* B **90** 165431
[52] Park C-H and Louie S G 2008 *Nano Lett.* **8** 2200–3
[53] Botello-Méndez A R, López-Urías F, Terrones M and Terrones H 2008 *Nano Lett.* **8** 1562–5
[54] Wang X and Dai H 2010 *Nat. Chem.* **2** 661–5
[55] Tapasztó L, Dobrik G, Lambin P and Biró L P 2008 *Nat. Nanotechnol.* **3** 397–401
[56] Sprinkle M, Ruan M, Hu Y, Hankinson J, Rubio-Roy M, Zhang B, Wu X, Berger C and de Heer W A 2010 *Nat. Nanotechnol.* **5** 727–31
[57] Wu C 2008 *Phys. Rev. Lett.* **101** 186807
[58] Hao X, Luo F, Zhai S, Meng Q, Wu J, Zhang L, Li T, Jia Y and Zhou M 2019 *Nano Futures* **3** 045002
[59] Canonico L M, Rappoport T G and Muniz R B 2019 *Phys. Rev. Lett.* **122** 196601
[60] Kresse G and Hafner J 1993 *Phys. Rev.* B **47** 558
[61] Kresse G and Furthmüller J 1996 *Comput. Mater. Sci.* **6** 15–50
[62] Perdew J P, Burke K and Ernzerhof M 1996 *Phys. Rev. Lett.* **77** 3865–8
[63] Heyd J, Scuseria G E and Ernzerhof M 2006 *J. Chem. Phys.* **124** 219906
[64] Koelling D D and Harmon B N 1977 *J. Phys. C: Solid State Phys.* **10** 3107
[65] Slater J C and Koster G F 1954 *Phys. Rev.* **94** 1498–524
[66] Li G, Hanke W, Hankiewicz E M, Reis F, Schäfer J, Claessen R, Wu C and Thomale R 2018 *Phys. Rev.* B **98** 165146
[67] Nevalaita J and Koskinen P 2018 *Phys. Rev.* B **97** 035411
[68] Nosé S 1984 *J. Chem. Phys.* **81** 511–9
[69] Hoover W G 1985 *Phys. Rev.* A **31** 1695–7
[70] Datta S 1995 *Electronic Transport in Mesoscopic Systems* (Cambridge University Press)
[71] Wimmer M 2009 Quantum transport in nanostructures: from computational concepts to spintronics in graphene and magnetic tunnel junctions *PhD Thesis* Universität Regensburg
[72] Groth C W, Wimmer M, Akhmerov A R and Waintal X 2014 *New J. Phys.* **16** 063065
[73] Thygesen K S, Bollinger M V and Jacobsen K W 2003 *Phys. Rev.* B **67** 115404
[74] Evers F and Mirlin A D 2008 *Rev. Mod. Phys.* **80** 1355–417